ACS OMEGA

Open Access

http://pubs.acs.org/journal/acsodf

Article

Directional and Orderly Arranged $Ni_{0.9}Mn_{0.1}(OH)_2$ Enables the Synthesis of Single-Crystal Ni-Rich Co-Free $LiNi_{0.9}Mn_{0.1}O_2$ with Enhanced Internal Structural Stability

Hailan Feng, Yuxing Xu, Yuncheng Zhou, Jiechen Song, and Qiangqiang Tan*

Cite This: *ACS Omega* 2024, 9, 6994−7002

Read Online

ACCESS | Metrics & More | Article Recommendations

ABSTRACT: In this paper, the effect of the structure characteristics of the precursor on the electrochemical properties of a single-crystal cobalt-free high-nickel $LiNi_{0.9}Mn_{0.1}O_2$ cathode is systematically studied. Precursors with different morphologies are synthesized by adjusting the coprecipitation reaction conditions. The results of SEM and XRD show that with the increase in the orderly stacking arrangement of internal primary nanosheets of $Ni_{0.9}Mn_{0.1}(OH)_2$, the exposed active {010} planes at the surface increase. The prepared cathode materials finally inherit the structural features of the precursor, and the single-crystal Co-free Ni-rich $LiNi_{0.9}Mn_{0.1}O_2$ cathode with highly exposed active {010} planes shows a well-ordered crystal structure and low Li^+/Ni^{2+} cation mixing. The characterization results reveal that the high percentage of {010} planes will improve the Li^+ transportation kinetics, decrease electrochemical impedance, and significantly alleviate the accumulation of rock-salt phases. Therefore, the material with this structure shows good electrochemical performance.

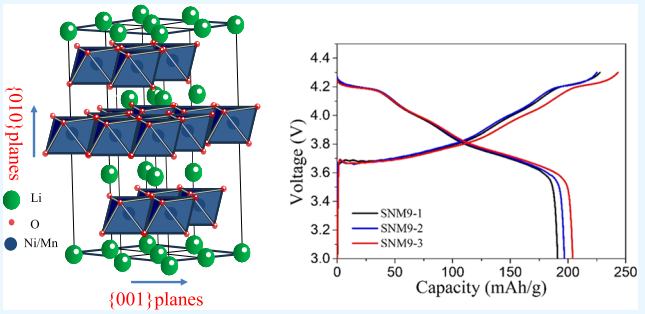

1. INTRODUCTION

In recent years, the application of new energy electric vehicles has developed rapidly, driven by the requirement for high-energy-density lithium-ion batteries (LIBs). High-nickel ternary materials such as Li $[Ni_xCo_yMn_z]$ O_2 (NCM, $x \geq 0.8$) are still the mainstream choice of battery cathode materials for electric vehicles.[1] However, due to the shortage of cobalt resources and price volatility, determining how to reduce and eliminate Co appears to be a formidable task. In 1992, Dahn's group first proposed a Co-free layered cathode $Li[Ni_xMn_{1-x}]O_2$ (NM, $0.5 \leq x < 1$) with a good discharge capacity and acceptable capacity retention;[2] then, increasing the Ni fraction in NM have attracted significant attention owing to high energy and low cost.[3−5]

The high-nickel polycrystalline cathode materials are prone to structural degradation, side reactions, and gas generation during long-term charging and discharging.[6] The single-crystal structure materials have unique characteristics,[7] exhibit high compact density, and display better structural stability and mechanical properties.[8,9] So single-crystal materials have become one of the most promising research directions of LIB cathode materials.[10] Particularly, increasing numbers of studies on single-crystalline $Li[Ni_xMn_{1-x}]O_2$ ($x \geq 0.9$) have been reported recently.[11] However, there are also many obvious disadvantages. (1) Slow Li^+ diffusion kinetics caused by the micron-sized particles of the SC-NM cathode lead to a relatively poor rate performance, and the lack of Co element is also the reason for the poor rate performance.[12] (2) The single-crystal cathode materials still undergo H2−H3 phase transition induced by anisotropic lattice strain in a highly lithium-depleted state.[13] (3) Moreover, it is difficult to synthesize large monodisperse single crystals.[14] The inner structure is considered a key factor to improve the performance of high-nickel cathode materials.[15] In particular, morphological regulation is an effective way to improve the Li^+ diffusion path by adjusting the structure and growth direction of internal primary particles.[16,17] For layered cathode materials with the α-$NaFeO_2$ structure, the close-packed structure of MO_2 oxygen layers(including NiO_6, CoO_6, and MnO_6 octahedron) perpendicular to the *c*-axis is related to the {001} lattice planes, including the (001) facets,[18] which prevents Li^+ deintercalation/intercalation.[19,20] However, the active planes {010} perpendicular to the {001} planes, including (010), (110), (100), and (100) facets, are beneficial to Li^+ diffusion because they provide good channels for Li^+

Received: November 5, 2023
Revised: January 9, 2024
Accepted: January 15, 2024
Published: February 5, 2024

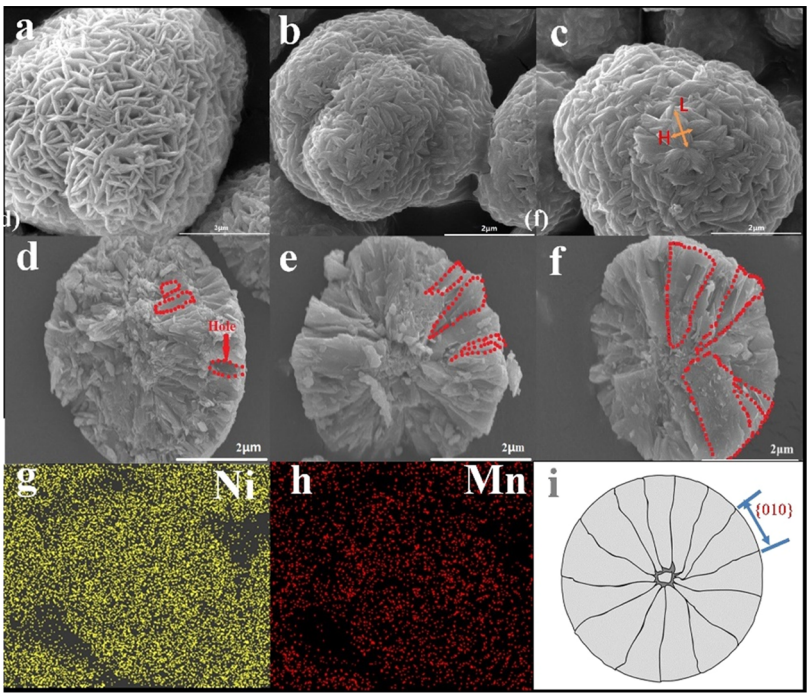

Figure 1. SEM images of (a) PNM9−1, (b) PNM9−2, and (c) PNM9−3. Cross-sectional SEM images of (d) PNM9−1, (e) PNM9−2, and (f) PNM9−3. (g, h) EDS images of the PNM9−3 sample. (i) Schematic diagram of the cross section of PNM9−3.

transport.[21,22] Many researchers have designed and prepared highly exposed {010} surfaces to improve the electrochemical performances of high-nickel cathode materials.[23−27] However, single-crystal cobalt-free high-nickel cathode materials have small particle sizes, making it difficult to synthesize precursors with high surface energy {010} planes, hindering the commercialization of single-crystal cobalt-free high-nickel cathode materials.

In this paper, we synthesized three precursors of $Ni_{0.9}Mn_{0.1}(OH)_2$ with different structural characteristics by morphology regulation. Impressively, when the degree of ordered arrangement increases, the exposed {010} planes increase, and the well-directional and orderly arranged cathode with highly exposed {010} planes presents superior rate capability and high cycling stability. This research increased our comprehension of the impact of the internal structural characteristics of precursors on the electrochemical properties of single-crystal cobalt-free high-nickel cathode materials.

2. EXPERIMENTAL SECTION

2.1. Preparation of Materials. The single-crystal Co-free Ni-rich cathode materials were prepared by coprecipitation and a high-temperature calcination method. The stoichiometric $NiSO_4{\cdot}6H_2O$ and $MnSO_4{\cdot}H_2O$ were dissolved in deionized water to form mixed metal salt solutions with 2.0 mol L^{-1}. A 10 mol L^{-1} NaOH solution and ammonia solutions were separately added into a reactor under the nitrogen atmosphere. The reaction temperature was controlled at 55 °C. The precursors were synthesized at pH values of 12.0, 11.8, and 11.6, and by adding 2.0, 3.0, and 4.0 mol L^{-1} ammonia solutions, labeled PNM9−1, PNM9−2, and PNM9−3, respectively. The precursor was filtered and washed and then dried at 120 °C in a vacuum oven for 10 h. The dried precursors were mixed with $LiOH{\cdot}H_2O$ in a Li/TM ratio of 1.05:1, and the cathode materials were heated at 870 °C in oxygen for 10 h, marked as SNM9−1, SNM9−2, and SNM9−3, respectively.

2.2. Characterizationof Materials. X-ray diffraction (XRD) was accomplished on a Shimadzu 7000S/L, with a scanning range of 10−80° and a step size of 2° min^{-1}. The morphologies and microstructural features of the samples were measured with scanning electron microscopy (SEM, Hitachi, S-4800) and transmission electron microscopy (TEM, FEI Tecnai F20). The surface elemental content of the powders was characterized by energy-dispersive X-ray spectroscopy (EDS). X-ray photoelectron spectroscopy was used to analyze the surface chemical valence states (XPS, Japan, AXIS SUPRA +). The particle size was analyzed on a laser diffraction instrument (Dandong Mastersizer 2000).

2.3. Electrochemical Tests. The electrochemical property of samples was performed using CR2025 half-cells. To obtain the electrode slurry, a 92 wt % active material, 5 wt % acetylene black, and 3 wt % poly(vinylidene difluoride) were mixed in *N*-methylpyrrolidinone. The CR2025 button battery was assembled with an electrode (cathode), Li metal as a reference electrode, a counter electrode, a separator (Celgard 2400 porous polypropylene film), and electrolytes (appropriate electrolyte of 1 M $LiPF_6$ in a mixture of EC/DMC/EMC). The charge−discharge performance was monitored on a Xinwei CT2001C (Shenzheng, China). The EIS (10^5−10^{-2} Hz) and the CV (scan rate of 0.1 mV s^{-1}) of the material were measured on an electrochemical workstation (CHI660E, Shanghai, China).

3. RESULTS AND DISCUSSION

The value of pH and the concentration of ammonia are the most important factors that affect the structure of NM hydroxides.[28] Three kinds of morphological characteristics of hydroxide $Ni_{0.9}Mn_{0.1}(OH)_2$ agglomerates were synthesized at different pH values and $NH_3{\cdot}H_2O$ contents. As shown in

https://doi.org/10.1021/acsomega.3c08782
ACS Omega 2024, 9, 6994−7002

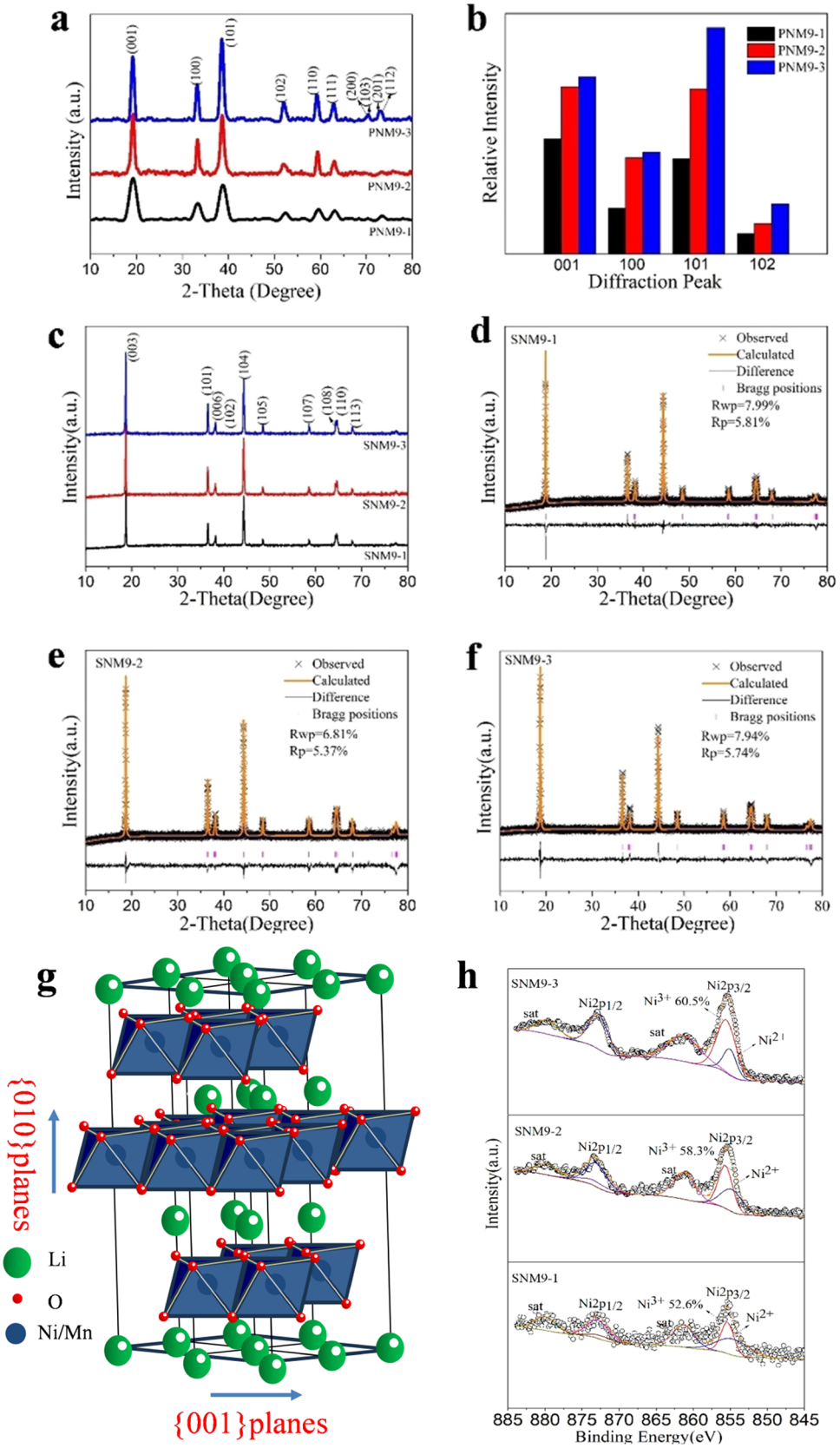

Figure 2. (a) XRD patterns of PNM9−1, PNM9−2, and PNM9−3. (b) Comparison of intensity for the diffraction peaks. (c) XRD patterns of the cathode material samples. XRD Rietveld refinement of (d) SNM9−1, (e) SNM9−2, and (f) SNM9−3. (g) Crystal structure of the SNM9 material. (h) XPS characterization of Ni 2p.

Figure. 1a−c, all precursors exhibit obvious secondary particles with the size of 3−4 μm, which are formed by aggregation of primary particles. With the decrease of the pH value and increase of the $NH_3{\cdot}H_2O$ content, the morphology of

https://doi.org/10.1021/acsomega.3c08782
ACS Omega 2024, 9, 6994−7002

Table 1. Rietveld Refinement Results of SNM9−1, SNM9−2, and SNM9−3

materials	a (Å)	c (Å)	c/a	$I_{(003)}/I_{(104)}$	Li^+/Ni^{2+} mixing (%)	R_{wp} (%)	R_p (%)
SNM9−1	2.8837	14.2235	4.9323	1.14	7.98	7.99	5.81
SNM9−2	2.8810	14.2142	4.9337	1.36	6.56	6.81	5.37
SNM9−3	2.8806	14.2130	4.9340	1.50	6.32	7.90	5.68

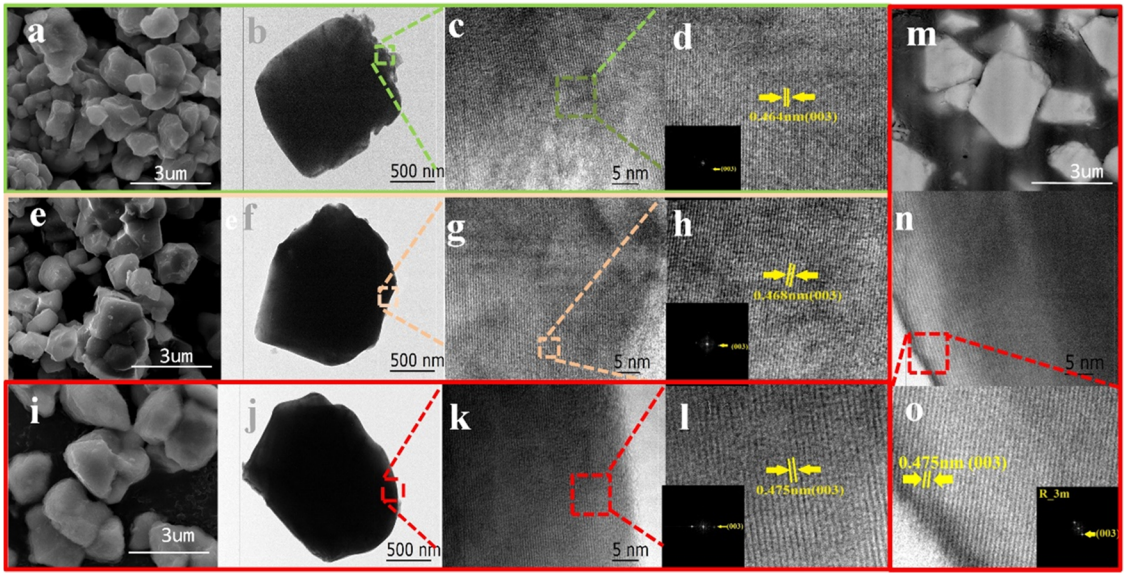

Figure 3. SEM, TEM, and HRTEM images of (a−d) SNM9−1, (e−h) SNM9−2, and (i−l) SNM9−3. Cross-sectional SEM, HRTEM, and the corresponding FFT images for SNM9−3 (m−o).

precursors changes from nanoneedle-like interweaved to nanosheet-like stacked, and the degree of the ordered arrangement gradually increases. Especially, the primary particles of PNM9-3 are arranged in an orderly direction. We found that the stacking thickness (H) of the primary particles increased gradually from PNM9-1 to PNM9-3, while the length (L) of the primary particles decreased. The increase of stacking thickness directly reflects that the active planes {010} are highly exposed to the surface of PNM9-3[21,29] because under the conditions of low pH values and high ammonia concentrations, the growth rate of the crystal is improved, while the nucleation rate is inhibited, so that the {001} plane of metal hydroxide octahedral evolving from nuclei is passivated, meaning the crystals tend to grow along the crystal plane lattice {010}.[30] In order to further analyze the internal structural characteristics of the precursor, a cross-sectional analysis was carried out. From the cross-sectional SEM images in Figure 1d−f, it can be observed that PNM9-3 nanosheets are orderly arranged and continuously along the direction from the center to the outer edge. While the internal distribution of PNM9-1 is disordered. The exposed surface is characterized by electrochemically active {010} planes, as the schematic diagram of the cross section of PNM9−3 shows that this orderly distribution structure is beneficial to increasing the Li^+ diffusion of the cathode materials.[31] EDS mapping images of PNM9−3 are displayed in Figure 1g,h, and Ni and Mn are uniformly distributed on the surface.

Figure 2 shows the XRD patterns of the PNM9−1, PNM9−2, PNM9−3, SNM9−1, SNM9−2, and SNM9−3. Figure 2a shows that all diffraction peaks of the precursors can be attributed to the β-$Ni(OH)_2$ structure, and no other impurity peaks are observed.[32,33] With the increase of the ammonia concentration and decrease in the pH value in the system, the peak intensities of all diffraction peaks increase. It can be noticed that the intensity of the (101) plane increases gradually. In particular, the intensity of the (101) peak of PNM9−3 is higher than that of the (001) peak (Figure 2b), which means that the crystal tends to grow along the c-axis, leading to the high exposure of the {010} plane.[22] This result is also consistent with the rule observed in the SEM images. Figure 2c displays the XRD patterns of the cathode material; all samples show the peaks of a typical hexagonal α-$NaFeO_2$ layered structure ($R\bar{3}m$ space group) without the impurity phase.[34] The Rietveld refinement results are summarized in Table 1. Compared with SNM9−1 and SNM9−2, lattice parameters a and c of SNM9−3 are smaller, which might be attributed to the radial arrangement of primary particles, further indicating that SNM9−3 prepared by the ordered intercalated precursor PNM9−3 has the best layered structure. Moreover, The I (0 0 3)/I (1 0 4) intensity ratio usually reflects the degree of the Li^+/ Ni^{2+} mixing.[35] The I (0 0 3)/I (1 0 4) intensity ratio of SNM9−3 is 1.50, which is higher than those of SNM9−1 (1.14) and SNM9−2 (1.36). In addition, the Li^+/ Ni^{2+} mixing degree of SNM9−3 is 6.32%, which is smaller than that of SNM9−1 (7.98%) and SNM9−2 (6.56%), thereby suggesting that a lower degree of Li^+/ Ni^{2+} mixing is present in SNM9−3. The main schematic crystal structure of the SNM9 material is illustrated in Figure 2g. When the material grows perpendicular to the c-axis, it is preferentially dominated by the {001} plane, which has no electrochemical activity for Li^+ transport. On the contrary, when it grows perpendicular to the b axis, it is indexed as the {010} plane, which is beneficial to Li^+ transport.

Figure 2h shows the XPS analysis of SNM9−1, SNM9−2 and SNM9−3 and exhibits the changes of the Ni chemical valence state. The Ni $2p_{3/2}$ peak can be divided into Ni^{2+} at

https://doi.org/10.1021/acsomega.3c08782
ACS Omega 2024, 9, 6994−7002

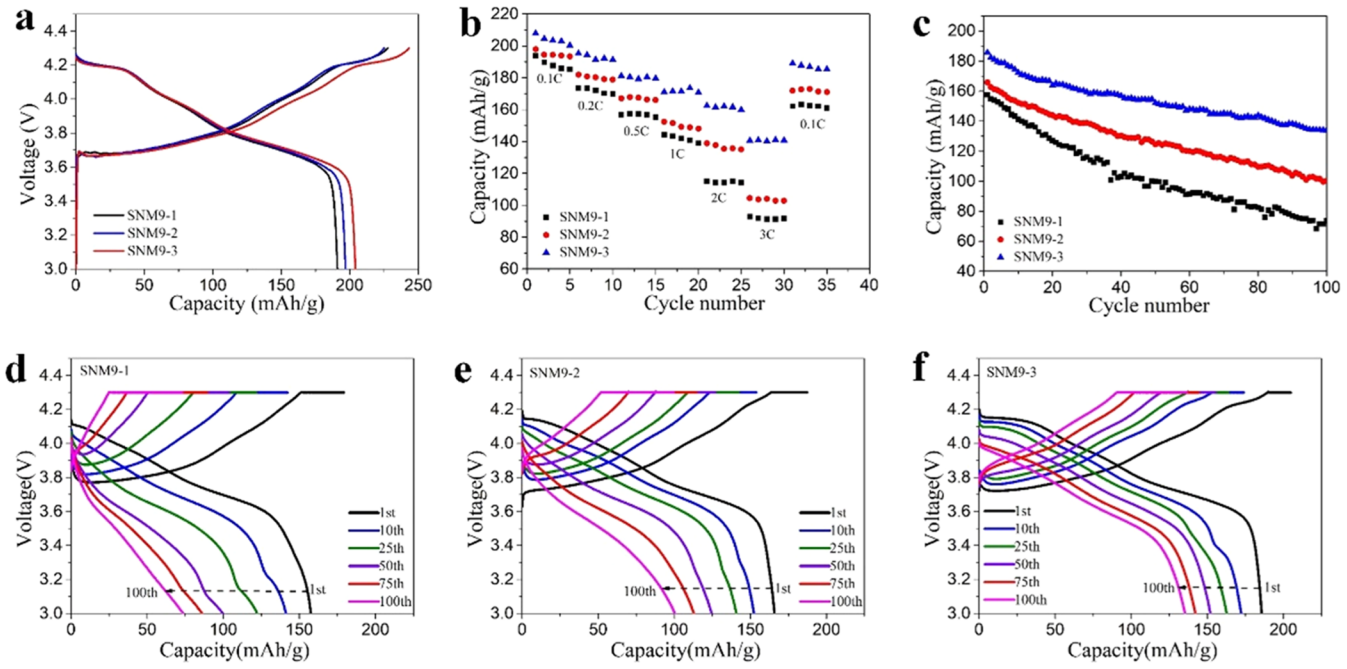

Figure 4. (a) Initial charge−discharge curves at 0.1 C in half-cells (3.0−4.3 V, vs Li^+/Li, 25 °C). (b) Rate performance at multiple current densities. (c) Cycling performances at 1 C. Charge−discharge curves at different cycles for (d) SNM9−1, (e) SNM9−2, and (f) SNM9−3.

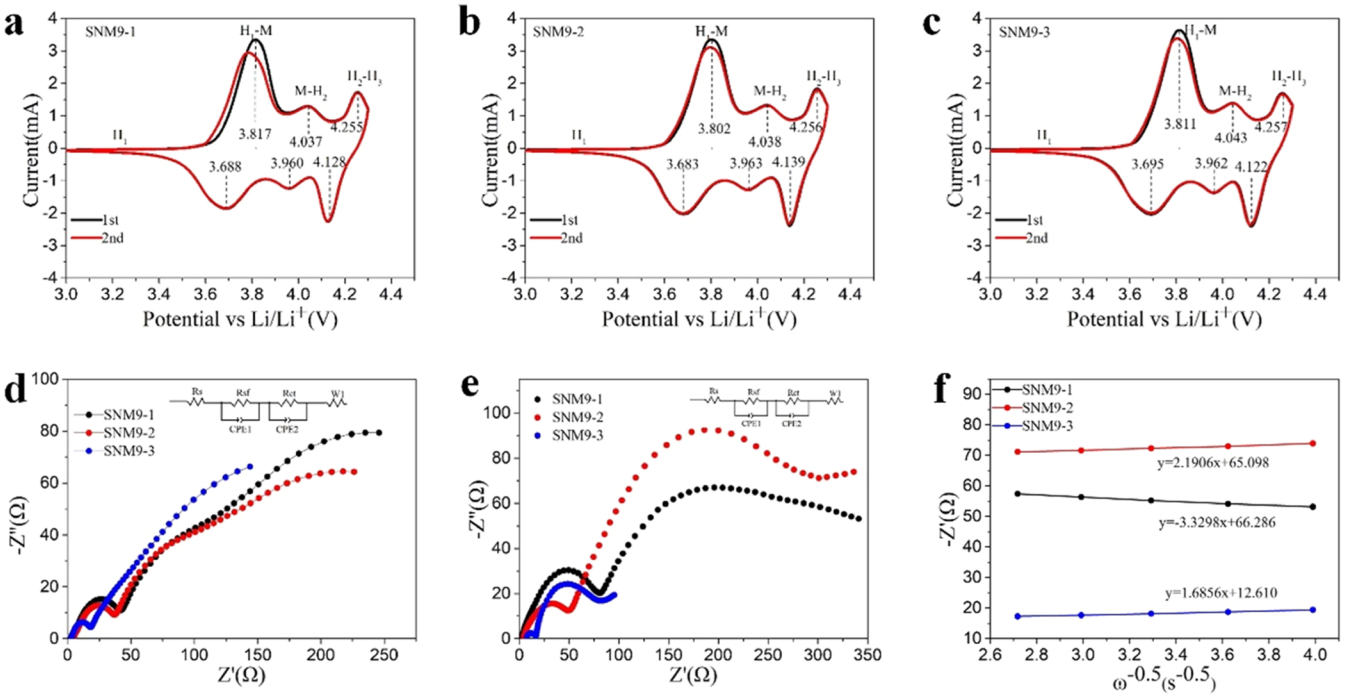

Figure 5. CV curves of (a) SNM9−1, (b) SNM9−2, and (c) SNM9−3. Nyquist plots of cathodes (d) the initial cycle and (e) after 100 cycles. (f) The profiles of Z' and $\omega^{-1/2}$.

around 854.7 eV and Ni^{3+} at around 855.8 eV.[39,40] SNM9−3 possesses a higher Ni^{3+} ratio of 60.5%, which is helpful in reducing the Li^+/Ni^{2+} mixing degree of SNM9−3.

After the solid-state calcination reaction, the precursors are transformed into single-crystal particles with a size of about 4 μm (Figure 3a,e,i). Meanwhile, TEM and HRTEM were used to analyze the morphology of SNM9−1, SNM9−2, and SNM9−3.For SNM9−3, the (003) lattice planes can be found clearly,[36] and the interplane spacing of SNM9−3 (0.475 nm) is larger than those of SNM9−1(0.464 nm) and SNM9−2(0.468 nm). Meanwhile, the FFT test results further confirm that the bright points indexed mainly refer to the (003) and (104) planes of the layered structure. These results indicate that this area belongs to {010} planes.[37,38] Therefore, combined with the results in Figure 1, we confirm that the percentage of the exposed active {010} planes of SNM9−3 is larger than those of SNM9−1 and SNM9−2. In order to analyze the internal morphology, the cross-sectional image of SNM9−3 is

https://doi.org/10.1021/acsomega.3c08782
ACS Omega 2024, 9, 6994−7002

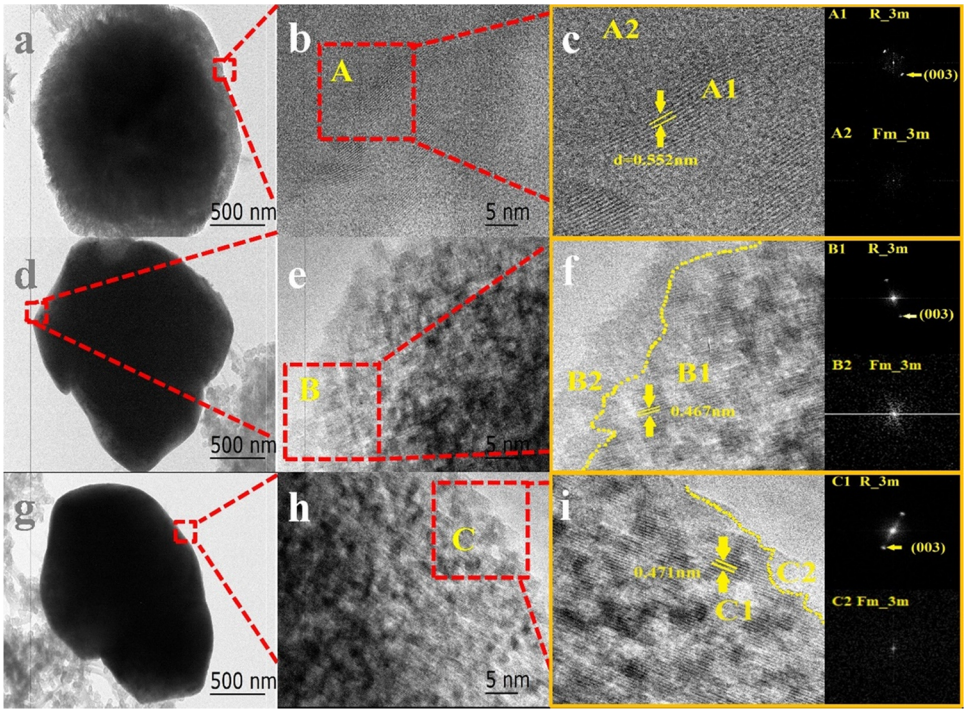

Figure 6. TEM and HRTEM images of (a–c) SNM9–1, (d–f) SNM9–2, and (g–i) SNM9–3 after 100 cycles.

displayed in Figure 3m. The individual particle is smooth without grain boundary. According to Figure 3o, an apparent interplanar spacing of 0.475 nm could also be measured, corresponding to the (003) lattice planes. We conclude that the electrochemically active {010} planes still exist after calcination. These results indicate that the structural characteristics of the final cathode materials can be successfully inherited from the growth orientation of precursors.

The electrochemical property of cathode materials was characterized and is exhibited in Figure 4. The initial discharge specific capacities of SNM9–1, SNM9–2, and SNM9–3 gradually increased from 191.0 mAh g^{-1} to 196.9 mAh g^{-1} and 204.1 mAh g^{-1}, respectively (Figure 4a). Higher Li^+/Ni^{2+} disorder hinders the migration of Li^+, leading to the lower initial discharge capacity of SNM9–1.[41,42] The initial Coulombic efficiencies are 83.8, 85.9, and 84.0%, respectively. SNM9–3 shows a lower cation mixing disorder, which is beneficial to Li^+ deintercalation. However, the large single particle size of SNM9–3 may affect the complete intercalation of Li^+, thus leading to a lower Coulombic efficiency. Figure 4b shows the rate performances at current densities of 0.1, 0.2, 0.5, 1, 2, and 3 C. Even at a high current density of 3 C, the reversible capacity of SNM9–3 remains as high as 140.0 mAh g^{-1}, exceeding the capacities of SNM9–2 (103.6 mAh g^{-1}) and SNM9–1(91.7 mAh g^{-1}). This can be ascribed to the fact that the unique ordered arrangement structure with a high percentage of exposed {010} planes facilitates the Li^+ diffusion inside the crystal.[38] In addition, the highest initial discharge capacity belongs to sample SNM9–3 (185.7 mAh g^{-1} at 1 C), while samples SNM9–2 and SNM9–1 showed 165.8 and 157.5 mAh g^{-1}, respectively. The capacity retention of SNM9–3 was 72.1% after 100 cycles, while that of SNM9–1 dropped rapidly to 60.5 and 47.3% (Figure 4c). SNM9–1 may suffer from serious undesirable electrode/electrolyte interface interaction, resulting in phase transition and electrolyte decomposition.[43,44] Figure 4d,e,f depicts the charge/discharge profiles of SNM9–1, SNM9–2 and SNM9–3 at 1 C from the first to the 100th cycle, respectively. SNM9–1 displays an obvious discharge voltage decrease, and the reversible capacity drops after long cycling. In contrast, the discharge voltage plateau of SNM9–3 is obviously higher than those of the SNM9–1 and SNM9–2 electrodes after 100 cycles. This implies that SNM9–3 has a better layered structure, which inhibits polarization during the charging/discharging process.

To further investigate the electrochemical reversibility during the cycling process, CV plots were performed at 0.1 mV s^{-1} (Figure 5a–c). Three redox oxidation peaks are composed of the phase change from H1 (hexagonal phase) to M (monoclinic phase), M to H2 (hexagonal phase), and H2 to H3 (hexagonal phase).[45,46] The potential interval (ΔE_p) between the oxidation and reduction peaks reflects the degree of electrode polarization during the charging and discharging process.[47,48] Compared with the ΔE_p of SNM9–1 (0.129 V) and SNM9–2 (0.119 V), the SNM9–3 material has a smaller redox potential difference (0.116 V). This means larger polarization and more irreversible capacity loss for SNM9–1, in line with its lower initial discharge capacity, which can be attributed to its slow migration rate of Li^+ owing to a disorder and fewer {010} active crystal planes compared with those of the SNM9–3 sample.

In addition, the effect of morphology regulation on electrochemical kinetics was studied by comparing the electrochemical impedance spectroscopy (EIS) analysis of SNM9–1, SNM9–2, and SNM9–3. Figure 5d,e shows the Nyquist plots of the first and after 100th cycles. The EIS spectra consist of two semicircles in the high-frequency regions and an inclined line in low-frequency regions. Clearly, the high-frequency region is related to the surface film (R_{sf}), the medium-frequency region is related to charge transfer impedance (R_{ct}), and the low-frequency region represents Warburg impedance (W), respectively.[49,50] Obviously, both the R_{sf} and R_{ct} of SNM9–1 and SNM9–2 are larger than those

https://doi.org/10.1021/acsomega.3c08782
ACS Omega 2024, 9, 6994–7002

of SNM9−3, which indicates that the orderly arranged structure with highly exposed {010} planes can effectively stabilize the crystal structure. The R_{ct} of SNM9−1 grows from 108 to 199 Ω after 100 cycles; however, SNM9−3 shows the lowest Rct (from 45 to 66 Ω). The increase in R_{sf} and R_{ct} is more apparent for SNM9−1 after 100 cycles, indicating that the material suffered from interfacial side reactions. On the contrary, the highly exposed {010} planes can effectively inhibit the interfacial reactions, reduce the internal impedance of the material, and facilitate the charge transport kinetics, which is good for electrochemical performance.

$$D_{Li}{}^{+} = \left(\frac{RT}{\sqrt{2}An^2F^2\sigma C}\right)^2 \quad (1)$$

$$Z' = R_s + R_{ct} + \sigma w^{-1/2} \quad (2)$$

The lithium-ion diffusion coefficient ($D_{Li}{}^{+}$) is calculated according to Formulas 1 and 2 to explain lithium-ion migration kinetics.[51] The value of σ can be calculated from the linear relationship of Z' and $\omega^{-1/2}$, as shown in Figure 5f.[52] After 100 cycles, the $D_{Li}{}^{+}$ values of the SNM9−1, SNM9−2 and SNM9−3 materials are 5.18×10^{-13}, 9.98×10^{-13}, and 1.98×10^{-12} $cm^2\ s^{-1}$, respectively. Obviously, the SNM9−3 sample exhibits a fast $D_{Li}{}^{+}$ diffusion rate, which is attributed to the highly ordered structure.

At the same time, the structure and phase transition of the cathode materials were studied after 100 cycles. As shown in Figure 6a, the surface of the SNM9−1 electrode is seriously corroded with more than 100 nm thickness, and most regions, such as A2, after the FFT transformation, are changed into $Fm\bar{3}m$ structures, indicating that the surface of SNM9−1 is almost transformed into the rock-salt phase. Such passive NiO-like phases substantially inhibit Li^+ transportation.[53] These factors contribute to the lower electrochemical performance. After 100 cycles, although the thin layer on the surface of SNM9−3 has a weak disordered rock-salt phase transition, (003) lattice spacing (0.471 nm) can be easily found in the subsurface and inner region. This further confirms that the ordered arrangement structure and a high percentage of exposed {010} planes can effectively alleviate the corrosion of the electrolyte to the cathode material and maintain a relatively good internal crystal structure.

4. CONCLUSIONS

In summary, by adjustment of the pH values and the ammonia concentrations, the primary particles gradually achieve a good directional arrangement, thus obtaining precursors with highly exposed {010} planes. The single-crystal cathode successfully inherited this grain orientation. The directionally ordered cathode materials have a good layered structure and low Li^+/Ni^{2+} mixing, affording efficient ion transport for fast Li^+ transport kinetics, leading to the improved electrochemical performance of the material. Such a good internal structure lays an important foundation for doping and coating modification to further improve the electrochemical performance of single-crystal Ni-rich, Co-free cathode materials.

AUTHOR INFORMATION

Corresponding Author

Qiangqiang Tan − *State Key Laboratory of Mesoscience and Engineering, Institute of Process Engineering, Chinese Academy of Sciences, Beijing 100190, China; Hebei Engineering Research Center of Power and Energy Storage Battery Materials, Hebei Technology Innovation Center of Advanced Energy Materials, Hebei Manufacturing Industry Innovation Center of New Energy Materials and Key Equipment, Langfang Technological Service Center of Green Industry, Langfang 065001, China;* orcid.org/0000-0001-5151-7251; Email: qtan@ipe.ac.cn

Authors

Hailan Feng − *State Key Laboratory of Mesoscience and Engineering, Institute of Process Engineering, Chinese Academy of Sciences, Beijing 100190, China; School of Chemical Engineering, University of Chinese Academy of Sciences, Beijing 100049, China; Hebei Engineering Research Center of Power and Energy Storage Battery Materials, Hebei Technology Innovation Center of Advanced Energy Materials, Hebei Manufacturing Industry Innovation Center of New Energy Materials and Key Equipment, Langfang Technological Service Center of Green Industry, Langfang 065001, China*

Yuxing Xu − *State Key Laboratory of Mesoscience and Engineering, Institute of Process Engineering, Chinese Academy of Sciences, Beijing 100190, China; Hebei Engineering Research Center of Power and Energy Storage Battery Materials, Hebei Technology Innovation Center of Advanced Energy Materials, Hebei Manufacturing Industry Innovation Center of New Energy Materials and Key Equipment, Langfang Technological Service Center of Green Industry, Langfang 065001, China*

Yuncheng Zhou − *State Key Laboratory of Mesoscience and Engineering, Institute of Process Engineering, Chinese Academy of Sciences, Beijing 100190, China; School of Chemical Engineering, University of Chinese Academy of Sciences, Beijing 100049, China; Hebei Engineering Research Center of Power and Energy Storage Battery Materials, Hebei Technology Innovation Center of Advanced Energy Materials, Hebei Manufacturing Industry Innovation Center of New Energy Materials and Key Equipment, Langfang Technological Service Center of Green Industry, Langfang 065001, China;* orcid.org/0000-0003-2398-5941

Jiechen Song − *State Key Laboratory of Mesoscience and Engineering, Institute of Process Engineering, Chinese Academy of Sciences, Beijing 100190, China; School of Chemical Engineering, University of Chinese Academy of Sciences, Beijing 100049, China; Hebei Engineering Research Center of Power and Energy Storage Battery Materials, Hebei Technology Innovation Center of Advanced Energy Materials, Hebei Manufacturing Industry Innovation Center of New Energy Materials and Key Equipment, Langfang Technological Service Center of Green Industry, Langfang 065001, China*

Complete contact information is available at: https://pubs.acs.org/10.1021/acsomega.3c08782

Notes

The authors declare no competing financial interest.

ACKNOWLEDGMENTS

This work was financially supported by the General Project of Beijing Natural Science Foundation (2222030), the Key R&D Projects in Gansu Province (22YF7GD193), and the research fund of State Key Laboratory of Mesoscience and Engineering (MESO-23-A06).

https://doi.org/10.1021/acsomega.3c08782
ACS Omega 2024, 9, 6994−7002

REFERENCES

(1) Lu, Y.; Zhang, Q.; Chen, J. Recent progress on lithium-ion batteries with high electrochemical performance. *Sci. China Chem.* **2019**, *62*, 533−548.

(2) Rossen, E.; Jones, C. D. W.; Dahn, J. R. Structure and electrochemistry of $Li_xMn_yNi_{1-y}O_2$. *Solid State Ionics* **1992**, *57*, 31−318.

(3) Liu, Y. L.; Wu, H. H.; Wang, Y. Q.; Li, K.; Yin, S.; Dahn, J. R. Impact of Shell Composition, Thickness and Heating Temperature on the Performance of Nickel-Rich Cobalt-Free Core-Shell Materials. *J. Electrochem. Soc.* **2020**, *167*, No. 160556.

(4) Sun, Y. K.; Lee, D. J.; Lee, Y. J.; Chen, Z. H.; Myung, S. T. Cobalt-Free Nickel Rich Layered Oxide Cathodes for Lithium-Ion Batteries. *ACS Appl. Mater. Interfaces* **2013**, *5*, 11434−11440.

(5) Ryu, H. H.; Sun, H. H.; Myung, S. T.; Yoon, C. S.; Sun, Y. K. Reducing cobalt from lithium-ion batteries for the electric vehicle era. *Energy Environ. Sci.* **2021**, *14*, 844−852.

(6) Liang, L.; Du, K.; Peng, Z.; Cao, Y.; Duan, J.; Jiang, J.; Hu, G. Co-precipitation synthesis of $Ni_{0.6}Co_{0.2}Mn_{0.2}(OH)_2$ precursor and characterization of $LiNi_{0.6}Co_{0.2}Mn_{0.2}O_2$ cathode material for secondary lithium batteries. *Electrochim. Acta* **2014**, *130*, 82−89.

(7) Reddy, M. V.; Rao, G. V. S.; Chowdari, B. V. R. Synthesis by molten salt and cathodic properties of Li $(Ni_{1/3}CO_{1/3}Mn_{1/3})$ O_2. *J. Power Sources* **2006**, *159* (1), 263−267.

(8) Han, X. Y.; Meng, Q. F.; Sun, T. L.; Sun, J. T. Preparation and electrochemical characterization of single-crystalline spherical Li-$Ni_{1/3}Co_{1/3}Mn_{1/3}O_2$ powders cathode material for Li-ion batteries. *J. Power Sources* **2010**, *195* (10), 3047−3052.

(9) Xu, X.; Huo, H.; Jian, J. Y.; Wang, L. G.; Zhu, H.; Xu, S.; He, X. S.; Yin, G. P.; Du, C. Y.; Sun, X. L. Radially oriented single-crystal primary nanosheets enable ultrahigh rate and cycling properties of $LiNi_{0.8}Co_{0.1}Mn_{0.1}O_2$ cathode material for lithium-ion batteries. *Adv. Energy Mater.* **2019**, *9*, No. 1803963.

(10) Langdon, J.; Manthiram, A. A. Perspective on Single-Crystal Layered Oxide Cathodes for Lithium-Ion Batteries. *Energy Storage Mater.* **2021**, *37*, 143−160.

(11) Ryu, H. H.; Lee, S. B.; Sun, Y. K. Promoting grain growth in Ni-rich single-crystal cathodes for high-performance lithium-ion batteries through Ce doping. *J. Solid State Electrochem.* **2022**, *26*, 2097−2105.

(12) Li, C.; Zhang, C.; Wang, K.; Yu, F.; Xie, J.; Zhang, Q. Multithiol- supported dicarboxylate-based metal-organic framework with excellent performance for lithium-ion battery. *Chem. Eng. J.* **2022**, *431*, No. 133234.

(13) Ryu, H. H.; Namkoong, B.; Kim, J. H.; Belharouak, I.; Yoon, C. S.; Sun, Y. K. Capacity fading mechanisms in Ni-rich single-crystal NCM cathodes. *ACS Energy Lett.* **2021**, *6*, 2726−2734.

(14) Han, X.; Meng, Q.; Sun, T.; Sun, J. Preparation and electrochemical characterization of single-crystalline spherical Li-$Ni_{1/3}Co_{1/3}Mn_{1/3}O_2$ powders cathode material for Li-ion batteries. *J. Power Sources* **2010**, *195* (10), 3047−3052.

(15) Yang, C. K.; Qi, L. Y.; Zuo, Z. C.; Wang, R. N.; Meng, Y.; Lu, J.; Zhou, H. H. Insights into the inner structure of high-nickel agglomerate as high-performance lithium-ion cathodes. *J. Power Sources* **2016**, *331*, 487−494.

(16) Xu, X.; Huo, H.; Jian, J. Y.; Wang, L. G.; Zhu, H.; Xu, S.; He, X. S.; Yin, G. P.; Du, C. Y.; Sun, X. L. Radially Oriented Single-Crystal Primary Nanosheets Enable Ultrahigh Rate and Cycling Properties of $LiNi_{0.8}Co_{0.1}Mn_{0.1}O_2$ Cathode Material for Lithium-Ion Batteries. *Adv. Energy Mater.* **2019**, *9*, No. 1803963.

(17) Du, F. H.; Zhou, Q.; Cao, H. S.; Dai, H.; Hu, D.; Sun, P. P.; Adkins, J.; Zheng, J. W. Confined growth of primary grains towards stabilizing integrated structure of Ni-rich materials. *J. Power Sources* **2020**, *478*, No. 228737.

(18) Zhang, X.; Zhang, P.; Zeng, T.; Yu, Z.; Qu, X.; Peng, X.; Zhou, Y. U.; Duan, X.; Dou, A.; Su, M.; Liu, Y. Improving the structure stability of $LiNi_{0.8}Co_{0.15}Al_{0.05}O_2$ by double modification of tantalum surface coating and doping. *ACS Appl. Energy Mater.* **2021**, *4* (8), 8641−8652.

(19) Chen, L.; Su, Y.; Chen, S.; Li, N.; Bao, L.; Li, W.; Wang, Z.; Wang, M.; Wu, F. Hierarchical $Li_{1.2}Ni_{0.2}Mn_{0.6}O_2$ nanoplates with exposed {010} planes as high-performance cathode material for lithium-ion batteries. *Adv. Mater.* **2014**, *26* (39), 6756−6760.

(20) Wei, G. Z.; Lu, X.; Ke, F. S.; Huang, L.; Li, J. T.; Wang, Z. X.; Zhou, Z. Y.; Sun, S. G. Crystal habit-tuned nanoplate material of $Li[Li_{1/3-2x/3}Ni_xMn_{2/3-x/3}]O_2$ for highrate performance lithium-ion batteries. *Adv. Mater.* **2010**, *22* (39), 4364−4367.

(21) Fu, F.; Xu, G. L.; Wang, Q.; Deng, Y. P.; Li, X.; Li, J. T.; Huang, L. S.; Sun, G. Synthesis of single crystalline hexagonal nanobricks of $LiNi_{1/3}Co_{1/3}Mn_{1/3}O_2$ with high percentage of exposed {010} active facets as high rate performance cathode material for lithium-ion battery. *J. Mater. Chem. A* **2013**, *1*, 3860−3864.

(22) Han, Y.; Shan, X.; Zhu, G.; Wang, Y.; Qu, Q.; Zheng, H. Hierarchically assembled $LiNi_{0.8}Co_{0.1}Mn_{0.1}O_2$ secondary particles with high exposure of {010} plane synthesized via co-precipitation method. *Electrochim. Acta* **2020**, *329*, No. 135057.

(23) Wu, F.; Tian, J.; Su, Y.; Wang, J.; Zhang, C.; Bao, L.; He, T.; Li, J.; Chen, S. Effect of Ni^{2+} Content on Lithium/Nickel Disorder for Ni- Rich Cathode Materials. *ACS Appl. Mater. Interfaces* **2015**, *7*, 7702−7708.

(24) Zhang, L. N.; Li, B.; Wu, H.; Xu, L.; Wang, X. Q.; Yang, F. Wu.; Wu, F. Sphere-shaped hierarchical cathode with enhanced growth of nanocrystal planes for high-rate and cycling-stable li-ion batteries. *Nano Lett.* **2015**, *15*, 656−661.

(25) Hua, W. B.; Liu, W. Y.; Chen, M. Z.; Indris, S.; Zheng, Z.; Guo, X. D.; Brunsb, M. T.; Wu, H.; Chen, Y. X.; Zhong, B. H.; Chou, S. L.; Kang, Y. M.; Ehrenberg, H. Unravelling the growth mechanism of hierarchically structured $Ni_{1/3}Co_{1/3}Mn_{1/3}(OH)_2$ and their application as precursors for high power cathode materials. *Electrochim. Acta* **2017**, *232*, 123−131.

(26) Yang, Y. S.; Xu, M.; Xie, M. B.; He, Y. H.; Huang, G. Y.; Yang, Y. C. Growth mechanisms for spherical mixed hydroxide agglomerates prepared by co-precipitation method: a case of $Ni_{1/3}Co_{1/3}Mn_{1/3}$ $(OH)_2$. *J. Alloys Comp.* **2015**, *619*, 846−853.

(27) Wei, G. Z.; Lu, X.; Ke, F. S.; Huang, L. J.; Li, T.; Wang, Z. X.; Zhou, Z. Y.; Sun, S. G. Crystal habit-tuned nanoplate material of Li $[Li_{1/3-2x/3}Ni_xMn_{2/3-x/3}]$ O_2 for high rate performance lithium-ion batteries. *Adv. Mater.* **2010**, *22* (39), 4364−4367.

(28) Su, Y. F.; Chen, G.; Chen, L.; Li, W. K.; Zhang, Q. Y.; Yang, Z. R.; Lu, Y.; Bao, L. Y.; Tan, J.; Chen, R. J.; Chen, S.; Wu, F. Exposing the {010} planes by oriented self-assembly with nanosheets to improve the electrochemical performances of Ni-rich Li $[Ni_{0.8}Co_{0.1}Mn_{0.1}]$ O_2 microspheres. *ACS Appl. Mater. Interfaces* **2018**, *10* (7), 6407−6414.

(29) Cheng, L.; Zhou, Y. N.; Zhang, B.; Wang, W.; Min, L.; Xiao, Z. M.; Ou, X. High-rate Ni-rich single-crystal cathodes with highly exposed {010} active planes through in-situ Zr doping. *Chem. Eng. J.* **2023**, *452*, No. 139336.

(30) Hua, W.; Liu, W.; Chen, M. S. I.; Indris, S.; Zheng, Z.; Zheng, Z.; Guo, X.; Guo, X.; Bruns, M.; Bruns, M.; Wu, T. H.; Wu, T. H.; Chen, Y.; Chen, Y.; Zhong, B.; Zhong, B.; Chou, S.; Chou, S.; Kang, Y. M.; Kang, Y. M.; Ehrenberg, H. Unravelling the growth mechanism of hierarchically structured $Ni_{1/3}Co_{1/3}Mn_{1/3}(OH)_2$ and their application as precursors for high-power cathode materials. *Electrochim. Acta* **2017**, *232*, 123−131.

(31) Yu, R.; Zhang, X. T.; Liu, X.; Xu, Y.; Huang, G.; Wang, X.; Wang, S. H.; Shu, H.; Yang, X. Hierarchically Structured Lithium-Rich Layered Oxide with Exposed Active {010} Planes as High-Rate-Capability Cathode for Lithium-Ion Batteries. *ACS Sustainable Chem. Eng.* **2017**, *5*, 8970−8981.

(32) Wang, Z. Y.; Zhang, Y. B.; Chen, J. C.; Lu, C. Study on decrystallization of cathode material and decomposition of electrolyte in $LiNi_{1/3}Co_{1/3}Mn_{1/3}O_2$-based cells. *J. Solid State Electrochem.* **2014**, *18* (6), 1757−1762.

(33) Langdon, J.; Manthiram, A. A perspective on single-crystal layered oxide cathodes for lithium-ion batteries. *Energy Storage Mater.* **2021**, *37*, 143−160.

https://doi.org/10.1021/acsomega.3c08782
ACS Omega 2024, 9, 6994−7002

(34) Shi, Y.; Zhang, M. H.; Meng, Y. S.; Chen, Z. Ambient-pressure relithiation of degraded $Li_xNi_{0.5}Co_{0.2}Mn_{0.3}O_2$ ($0 < x < 1$) via eutectic solutions for direct regeneration of lithium-ion battery cathodes. *Adv. Energy Mater.* **2019**, *9*, No. 1900454.
(35) Xiao, L.; Yang, Y.; Zhao, Y.; et al. Synthesis and electrochemical properties of submicron $LiNi_{0.8}Co_{0.2}O_2$ by a polymer-pyrolysis method. *Electrochim. Acta* **2008**, *53*, 3007−3012.
(36) Liu, W.; Li, J. X.; Li, W. T.; Xu, H. Y.; Zhang, C.; Qiu, X. P. Inhibition of transition metals dissolution in cobalt-free cathode with ultrathin robust interphase in concentrated electrolyte. *Nat. Commun.* **2020**, *11*, No. 3629.
(37) Zeng, J.; Cui, Y. H.; Qu, D. Y.; Zhang, Q.; Wu, J. W.; Zhu, X. M.; Li, Z. H.; Zhang, X. H. Facile synthesis of platelike hierarchical $Li_{1.2}Mn_{0.54}Ni_{0.13}Co_{0.13}O_2$ with exposed {010} planes for high-rate and long cycling-stable lithium ion batteries. *ACS Appl. Mater. Interfaces* **2016**, *8*, 26082−26090.
(38) Su, Y. F.; Chen, G.; Chen, L.; et al. Exposing the {010} Planes by Oriented Self-Assembly with Nanosheets To Improve the Electrochemical Performances of Ni-Rich $Li[Ni_{0.8}Co_{0.1}Mn_{0.1}]O_2$ Microspheres. *ACS Appl. Mater. Interfaces* **2018**, *10*, 6407−6414.
(39) Shang, G.; Tang, Y.; Lai, Y.; Wu, J.; Yang, X.; Li, H.; Peng, C.; Zheng, J.; Zhang, Z. Enhancing structural stability unto 4.5 V of ni-rich cathodes by tungsten-doping for lithium storage. *J. Power Sources* **2019**, *423*, 246−254.
(40) Huang, Y.; Liu, Y.; Liu, X.; Yu, X.; Yu, R.; Cao, R.; Cao, S.; Pei, S.; Pei, Y.; Luo, Y. Z.; Luo, Z.; Zhao, Q.; Zhao, Q.; Chang, B.; Chang, B.; Wang, Y.; Wang, X. Tellurium Surface Doping to Enhance the Structural Stability and Electrochemical Performance of Layered Ni-Rich Cathodes. *ACS Appl. Mater. Interfaces* **2019**, *11*, 40022−40033.
(41) Wang, T. X.; Yuan, M. L.; Xie, S.; Liu, J. J.; Yan, J. Q.; Li, Z.; Peng, J. Synergistic effect of Al−B co-doping to boost the $LiNi_{0.9}Co_{0.05}Mn_{0.05}O_2$ properties in lithium-ion batteries. *Ceram. Int.* **2022**, *48*, 20605−20611.
(42) Ryu, H. H.; Park, K. J.; Yoon, C. S.; Sun, Y. K. Capacity Fading of Ni-Rich Li $[Ni_xCo_yMn_{1-x-y}]$ O_2 ($0.6 \leq x \leq 0.95$) Cathodes for High-Energy-Density Lithium- Ion Batteries: Bulk or Surface Degradation. *Chem. Mater.* **2018**, *30*, 1155−1163.
(43) Zhao, Z. Y.; Huang, B.; Wang, M.; Yang, X. W.; Gu, Y. J. Facile synthesis of fluorine doped single crystal Ni-rich cathode material for lithium-ion batteries. *Solid State Ionics* **2019**, *342*, 115065.
(44) Hu, G.; Li, L.; Lu, Y.; Cao, Y.; Peng, Z.; Xue, Z.; Zhang, Y.; Fan, J.; Du, K. $SrCO_3$ assisted synthesis of disk-like micron-sized monocrystalline $LiNi_{0.5}Co_{0.2}Mn_{0.3}O_2$ with Preferred (104) plane and its enhanced cycle performance. *J. Electrochem. Soc.* **2020**, *167*, No. 140505.
(45) Robert, R.; Bünzli, C.; Berg, E.; Nov′ak, J. P. Activation mechanism of $LiNi_{0.80}Co_{0.15}Al_{0.05}O_2$: Surface and bulk operando electrochemical, differential electrochemical mass spectrometry, and x-ray diffraction analyses. *Chem. Mater.* **2015**, *27*, 526−536.
(46) Yang, X.; Tang, Y. G.; Shang, J.; Wu, Y.; Lai, J.; Li, Y.; Qu, Z.; Zhang, Z. Enhanced cyclability and high-rate capability of $LiNi_{0.88}Co_{0.095}Mn_{0.025}O_2$ cathodes by homogeneous Al^{3+} doping. *ACS Appl. Mater. Interfaces* **2019**, *11*, 32015−32024.
(47) Zheng, J. C.; Yang, Z.; He, Z. J.; Tong, H. W.; Yu, J.; Zhang, J. F. In situ formed $LiNi_{0.8}Co_{0.15}Al_{0.05}O_2$@$Li_4SiO_4$ composite cathode material with high rate capability and long cycling stability for lithium-ion batteries. *Nano Energy* **2018**, *53*, 613−621.
(48) Cheng, L.; Zhou, Y. A.; Zhang, B.; Wang, W.; Ming, L.; Xiao, Z. M.; Ou, X. High-rate Ni-rich single-crystal cathodes with highly exposed {010} active planes through in-situ Zr doping. *Chem. Eng. J.* **2023**, *452*, No. 139336.
(49) Ni, L.; Chen, H.; Deng, W.; Wang, B.; Chen, J.; Mei, Y.; Zou, G.; Hou, H.; Guo, R.; Xie, J.; Ji, X. Atomical reconstruction and cationic reordering for nickel-rich layered cathodes. *Adv. Energy Mater.* **2022**, *12*, No. 2103757.
(50) Zhu, F.; Shi, Y.; Hu, G.; Peng, Z.; Cao, Y.; Sun, Q.; Xue, Z.; Zhang, Y.; Du, K. Enhanced electrochemical performance of $LiNi_{0.8}Co_{0.1}Mn_{0.1}O_2$ via titanium and boron co-doping. *Ceram. Int.* **2021**, *47*, 3070−3078.
(51) Zhang, Z.; Chen, D.; Chang, C. Improved electrochemical performance of $LiNi_{0.8}Co_{0.1}Mn_{0.1}O_2$ cathode materials via incorporation of rubidium cations into the original Li sites. *RSC Adv.* **2017**, *7*, 51721−51728.
(52) Zhao, T.; Meng, Y.; Ji, R.; Wu, F.; Li, L.; Chen, R. Maintaining structure and voltage stability of Li-rich cathode materials by green water-soluble binders containing Na^+ ions. *J. Alloys Compd.* **2019**, *811*, No. 152060.
(53) Fan, X. M.; Ou, X.; Zhao, W. G.; Liu, Y.; Zhang, B.; Zhang, J. F.; Zou, L. F.; Seid, L.; Li, Y. Z.; Hu, G. R.; Battaglia, C.; Yang, Y. In situ inorganic conductive network formation in high-voltage single-crystal Ni-rich cathodes. *Nat. Commun.* **2021**, *12*, No. 5320.

https://doi.org/10.1021/acsomega.3c08782
ACS Omega 2024, 9, 6994−7002